Supporting Information for: Nanoscale imaging of current density with a single-spin magnetometer

K. Chang, A. Eichler, J. Rhensius, L. Lorenzelli, and C. L. Degen*

Department of Physics, ETH Zurich, Otto Stern Weg 1, 8093 Zurich, Switzerland

* correspondence to: degenc@ethz.ch

I. MEASUREMENT APPARATUS

A. Microscope

Experiments were carried out at room temperature with a home-built combined AFM/confocal microscope. Cantilever detection in the AFM was done by laser deflection using a 980 nm pig-tail diode laser and detected by a four quadrant photodiode (Hamamatsu S2044). Photodiode signals were amplified by a current amplifier (HF2CA, Zurich Instruments). Signal modulation and feedback control were done by a lock-in amplifier (HF2LI, Zurich Instruments). Scanning and z-feedback were done by a closed-loop three-axis piezo stage (Physik Instrumente) and data acquisition was done by a standard DAQ card (NI PCIe-6353).

NV centers were excited by $< 100\,\mu$W, 532 nm laser light in a transmission arrangement. A high numerical aperture objective (Olympus IUS2, N.A.=0.9) was approached to the NV probes from below the sample. Luminescent photons were collected by an avalanche photodiode over an effective filter bandwidth of 630-800 nm. Microwaves were generated by a signal generator (Quicksyn FSW-0020) and pulses were generated by a TTL microwave switch (ZYSWA-2-50DR, Mini-Circuits) with the TTL pulses generated by a PCI pulse generator (PulseBlasterESR-PRO, Spincore).

To apply a current through the nanowires and nanotubes, an arbitrary waveform generator (Agilent 33220A, 20 MHz) was used as the source. A 10 kΩ shunt resistor was placed in series with the devices to both monitor and limit the current. The current was modulated between a positive current and negative current of the same amplitude at 1 kHz in a square wave pattern.

B. Scanning NV tips

The scanning NV probes were prepared by attaching nanodiamonds hosting single NV centers (DiaScence 25, 0.44 mg/mL) to commercial AFM cantilever (ATEC-NC, NANOSENSORS). The nanodiamonds had a nominal diameter of 25 nm and typically contained 1-2 NV centers per crystal. To attach the nanodiamonds, the tip of a cantilever was first coated with an aqueous solution of 0.1 wt% poly-L-lysine (Sigma-Aldrich). Then, nanodiamonds were dispersed at low density on the surface of a quartz cover slip so that single NV center could be resolved optically and single crystals could be located with the AFM. By correlating the optical and topographic images, nanocrystals with single NV centers were identified. To attach a nanocrystal, the AFM tip was maneuvered over the crystal and brought into contact.

To determine the orientation of the attached NV center, EPR spectra were taken at a few different relative xyz positions of an external polarizing magnet. The resulting EPR frequencies were used to calculate the angles θ and ϕ by least squares regression. We know from separate measurements (e.g. Ref. [S1]) that the error between the fitted NV orientation and the true NV orientation is a few degrees at most.

C. Current-carrying devices

Metallic nanowires were fabricated on 150-180- μm-thick quartz coverslips (Electron Microscopy Science 72256-08). The structures were defined by electron beam lithography with a tri-layer resist consisting of PMMA 50K, PMMA 950K, and the conductive polymer ESPACER 300Z (Showa Denko K.K.). The metal structures were deposited by electron beam evaporation and consisted of 3 nm Cr and 97 nm Pt. The resist was removed by a standard lift-off process in NMP at 80° C for 2 hours.

Carbon nanotubes were grown by first preparing a Si substrate by depositing 20 nm thick AlOx (ALD) followed by an 0.4 nm thick layer of Fe (e-beam evaporation). CNT growth on the substrate was done in a vertical CVD reactor (Black Magic ProTM, Aixtron) using the rapid heating cold-wall method [S2]. The growth was done at 740° C with 800 sccm Ar and 10 sccm C_2H_2 and at a chamber pressure of 0.2 mbar. The resulting vertically aligned CNT were then suspended in IPA and spread onto a quartz coverslip by dip coating. Metal contacts were defined by the same e-beam

lithography steps described with the metallic nanowires. The metallic contacts consisted of 0.5 nm Cr and 100 nm Pd deposited by electron beam evaporation. Finally, the resist was removed by lift off in acetone at 40° C for 2 hours.

II. MEASUREMENT PROTOCOL

A. Fitting of EPR spectra

EPR spectra were fitted using a Lorentzian function,

$$y(\omega) = 1 - \epsilon \frac{1}{[(\omega - \omega_{\text{peak}})/\Omega]^2 + 1} \ . \tag{S1}$$

This fit yielded three parameters, the peak position ω_{peak}, line width parameter Ω and optical contrast ϵ.

The peak position ω_{peak} was used to extract the component of the DC magnetic field that is parallel to the NV symmetry axis $\mathbf{n}$. We converted it to units of magnetic field (Tesla) as

$$B_{||} = |\mathbf{B}_{\text{dc}} \cdot \mathbf{n}| = \frac{|\omega_{\text{peak}} - D|}{\gamma} \ , \tag{S2}$$

where $D = 2870\,\text{MHz}$ is the zero-field splitting parameter and $\gamma = 28\,\text{GHz/T}$ is the electron gyromagnetic ratio [S3]. (We used units of Hz for all frequencies). $B_{||}$ has contributions from the Oersted magnetic field, local or external static magnetic fields, and is affected by temperature drifts due to the temperature dependence of D. To determine the Oersted contribution to $B_{||}$, two spectra were recorded with positive and negative current applied. The differential line shift $\delta\omega$, given by

$$\delta\omega = \tfrac{1}{2}(\omega_{+I} - \omega_{-I}) \ , \tag{S3}$$

is then directly proportional to the current-induced field,

$$B_{\text{current}} = \frac{\delta\omega}{\gamma} \ . \tag{S4}$$

Likewise, the center frequency

$$\omega_0 = \tfrac{1}{2}(\omega_{+I} + \omega_{-I}) \tag{S5}$$

provided a separate measurement (without the Oersted contribution) of the static magnetic field,

$$B_{\text{static}} = \frac{|\omega_0 - D|}{\gamma} \ . \tag{S6}$$

The line width parameter Ω and optical contrast ϵ were used to extract the component of the microwave magnetic field that is transverse to the NV symmetry axis $\mathbf{n}$,

$$B_\perp = |\mathbf{B}_{\rm mw} \times \mathbf{n}| = \frac{\sqrt{2}\omega_1}{\gamma} \tag{S7}$$

where ω_1 is the Rabi frequency and the factor of $\sqrt{2}$ is due to the rotating wave approximation and the spin-1 nature of the NV center [S4]. The line width parameter Ω and optical contrast ϵ depend on ω_1 approximately as

$$\Omega = (\omega_1^2 + \Omega_{\rm min}^2)^{1/2} \ , \tag{S8}$$

$$\epsilon = \epsilon_{\rm max} \frac{\omega_1^2}{\omega_1^2 + \Omega_{\rm min}^2} \ . \tag{S9}$$

Here, $\Omega_{\rm min}$ is the minimum EPR linewidth for low microwave power. In our experiments, $\Omega_{\rm min}$ was limited by the laser [S5, S6] or magnetic linebroadening due to paramagnetic impurities in the diamond nanocrystals, and was typically around $2-5\,$MHz. $\epsilon_{\rm max}$ is the maximum optical contrast observed at high microwave powers (under saturation) with typical values between $0.2-0.3$. The two equations can be combined to determine $B_\perp$ from a (Ω, ϵ) dataset,

$$B_\perp = \frac{\sqrt{2}\omega_1}{\gamma} = \frac{\sqrt{2}\Omega}{\gamma}\sqrt{\frac{\epsilon}{\epsilon_{\rm max}}} \ . \tag{S10}$$

For the reported experiments, we have used the average values for Ω and ϵ from the positive/negative current EPR spectra.

Eqs. (S8) and (S9) have limiting cases for low and high microwave power that we have used in our analysis. For the metallic wire samples, $\epsilon_{\rm max}$ changes locally due to the transmission arrangement and laser reflection from the wire. In these samples, high microwave power above the saturation threshold ($\omega_1 > \Omega_{\rm min}$) is applied and the EPR contrast is approximately constant $\epsilon \approx \epsilon_{\rm max}$ while the linewidth varies as $\Omega \approx \omega_1 \propto B_\perp$. For the carbon nanotube sample, $\epsilon_{\rm max}$ remains constant. In this case low microwave power below the saturation threshold of the EPR resonance ($\omega_1 < \Omega_{\rm min}$) is applied and the linewidth is approximately constant ($\Omega \approx \Omega_{\rm min}$). The contrast varies as $\epsilon \propto \omega_1^2 \propto B_\perp^2$ with these parameters.

B. Sensitivity of DC vs. microwave detection

We have compared how sensitively the EPR spectrum [Eq. (S1)] responds to changes in DC or microwave fields. A useful figure of merit is the change in the optical signal y in response to a

change in ω_{peak} or ω_1, respectively. For DC detection, the maximum change in y in response to a change in ω_{peak} occurs when the microwave frequency ω is tuned to the point of maximum slope, $\omega - \omega_{\text{peak}} = \pm\Omega/\sqrt{3}$, where

$$\left.\frac{\partial y}{\partial \omega_{\text{peak}}}\right|_{\omega=\omega_{\text{peak}}-\frac{\Omega}{\sqrt{3}}} = -\frac{3\sqrt{3}\epsilon}{8\Omega} = -\frac{3\sqrt{3}\epsilon_{\text{max}}\omega_1^2}{8(\Omega_{\text{min}}^2+\omega_1^2)^{3/2}} \ . \tag{S11}$$

This equation has a maximum at $\omega_1 = \sqrt{2}\Omega_{\text{min}}$ where it takes a value of $\epsilon_{\text{max}}/(4\Omega_{\text{min}}) = 0.25\epsilon_{\text{max}}/\Omega_{\text{min}}$ (see Fig. S1).

For microwave detection via the linewidth parameter Ω, the maximum change in y again occurs at the point of maximum slope, where

$$\left.\frac{\partial y}{\partial \omega_1}\right|_{\omega=\omega_{\text{peak}}-\frac{\Omega}{\sqrt{3}}} = -\frac{3\epsilon_{\text{max}}\Omega_{\text{min}}^2\omega_1}{2(\Omega_{\text{min}}^2+\omega_1^2)^2} \ . \tag{S12}$$

Here, the maximum is at $\omega_1 = \Omega_{\text{min}}/\sqrt{3}$ with a value of $9\sqrt{3}\epsilon_{\text{max}}/(32\Omega_{\text{min}}) \approx 0.49\epsilon_{\text{max}}/\Omega_{\text{min}}$.

For microwave detection via the optical contrast ϵ, the maximum change in y occurs at $\omega = \omega_{\text{peak}}$, and

$$\left.\frac{\partial y}{\partial \omega_1}\right|_{\omega=\omega_{\text{peak}}} = -\frac{2\epsilon_{\text{max}}\Omega_{\text{min}}^2\omega_1}{(\Omega_{\text{min}}^2+\omega_1^2)^2} \ . \tag{S13}$$

Here, the maximum is at $\omega_1 = \Omega_{\text{min}}/\sqrt{3}$ with a value of $3\sqrt{3}\epsilon_{\text{max}}/(8\Omega_{\text{min}}) \approx 0.65\epsilon_{\text{max}}/\Omega_{\text{min}}$.

The three detection methods are compared in Fig. S1, which plots the respective derivatives of y as a function of ω_1 for fixed values of Ω_{min} and ϵ_{max}. The figure clearly shows that the measurement is more sensitive to microwave fields in the low-field regime ($\omega_1 \lesssim \Omega_{\text{min}}$) while it is more sensitive to DC fields in the high-field regime. Considering that $\delta\omega = \gamma B_{||}$ and $\omega_1 = 1/\sqrt{2}\gamma B_\perp$, the maximum responsivity to microwave fields $B_\perp$ in contrast detection is $\sim 1.8\times$ the maximum sensitivity to DC fields $B_{||}$.

C. Fitting of line scans

Line scans across straight sections of nanowires or nanotubes were used to determine the separation z between the NV center and the surface of the conductor. The conductor was modeled by an infinitely long, thin wire. The analytical magnetic field is given by

$$\mathbf{B} = \frac{\mu_0 I}{2\pi[(x-x_0)^2+d^2]}(d, 0, -x+x_0) \tag{S14}$$

where the wire runs along y, the scan is performed along x, the wire is located at x_0, and d is the vertical distance between the center of the wire and the NV center. The DC magnetic field

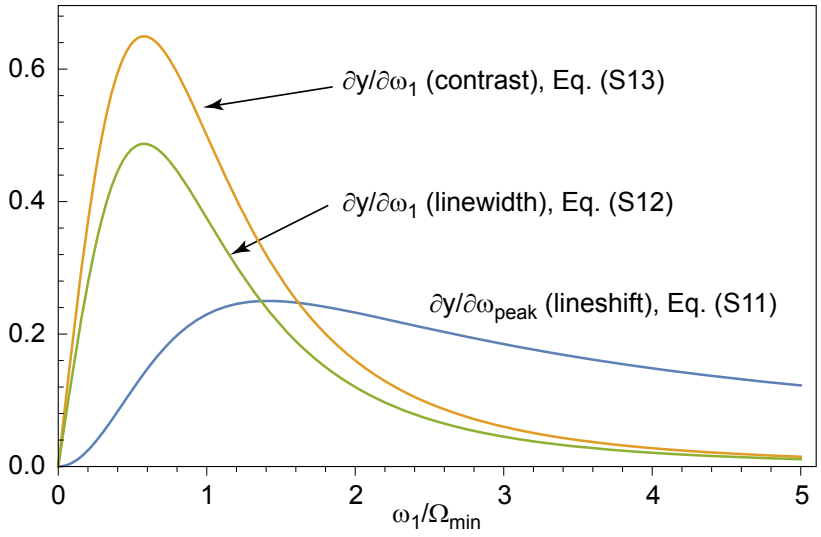

FIG. S1. Responsivity of y to changes in ω_{peak} and ω_1 (absolute values). Vertical axis has units of contrast per Ω_{min}. ϵ_{max} was set to 1.

detected by the NV center is

$$B_{||} = \mathbf{B}_{\mathrm{dc}} \cdot \mathbf{n} = \frac{\mu_0 I[e_x d - e_z(x - x_0)]}{2\pi((x - x_0)^2 + d^2)} \tag{S15}$$

where $\mathbf{n} = (e_x, e_y, e_z) = (\sin\theta\cos\phi, \sin\theta\sin\phi, \cos\theta)$ is a unit vector pointing along the NV quantization axis. The tip stand-off z, which is the vertical distance between the top of the conductor and the NV center, is then given by $z = d - h/2$ where h is the conductor height.

To check the accuracy of our infinite wire model, we compared it with the simulated magnetic field of a square wire. The simulation was done in COMSOL with a square cross section of 100 nm by 100 nm and a sampling step of 5 nm (Fig. S2). The result of the simulation agrees with the infinite wire model better than 94% even for the closest investigated distance of $z = 25\,\mathrm{nm}$. We have therefore used the infinite wire model to infer the stand-off distance z for all experiments reported in this work.

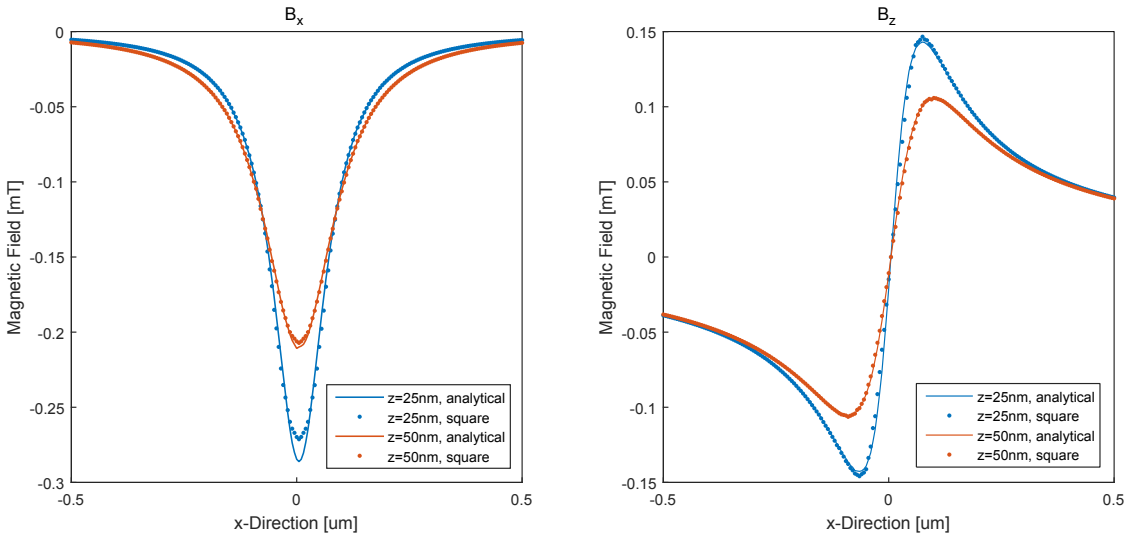

FIG. S2. COMSOL simulation of a square wire with a 100 nm by 100 nm cross-section (dots) and the analytical solution of an infinitely thin wire (solid line). Sampling step is 5 nm. Current is 100 μA in the $-y$ direction.

III. RECONSTRUCTION OF CURRENT DENSITY

A. Deconvolution

To reconstruct the two-dimensional current density $\mathbf{J}(x, y)$ from a two-dimensional magnetic field map $B_{||}(x, y)$ or $B_{\perp}(x, y)$, we adapted an inverse filtering technique described by Roth et al. [S7]. In two-dimensional Fourier space, the Biot-Savart law is

$$B_x(k_x, k_y, z) = +g(k_x, k_y, z) J_y(k_x, k_y) \ , \tag{S16}$$

$$B_y(k_x, k_y, z) = -g(k_x, k_y, z) J_x(k_x, k_y) \ , \tag{S17}$$

$$B_z(k_x, k_y, z) = ig(k_x, k_y, z) \left(\frac{k_y}{k} J_x(k_x, k_y) - \frac{k_x}{k} J_y(k_x, k_y) \right) \ , \tag{S18}$$

where k_x and k_y are the k-vectors associated with x and y, and $k = |\mathbf{k}| = (k_x^2 + k_y^2)^{1/2}$. The function

$$g(k_x, k_y, z) = \frac{\mu_0 h_{\text{eff}}}{2} e^{-kz} \tag{S19}$$

is a Green's function and

$$h_{\text{eff}} = \frac{1 - e^{-kh}}{k} \tag{S20}$$

is an effective thickness of the conductor. h is the real physical thickness of the conductor. The magnetic field parallel to the NV axis is

$$B_{||} = \mathbf{B}\cdot\mathbf{n} \tag{S21}$$

$$= g\left[e_x J_y - e_y J_x + ie_z\left(\frac{k_y}{k}J_x - \frac{k_x}{k}J_y\right)\right]$$

$$= g\left[\left(e_x - ie_z\frac{k_x}{k}\right)J_y - \left(e_y - ie_z\frac{k_y}{k}\right)J_x\right] \tag{S22}$$

and the magnetic field transverse to the NV axis is

$$B_\perp^2 = |\mathbf{B}\times\mathbf{n}|^2 = \left(|\mathbf{B}|^2 - B_{||}^2\right)^{1/2} \tag{S23}$$

$$= g^2\left(\left[e_x^2\frac{k_x^2}{k^2} - e_y^2\frac{k_y^2}{k^2} + e_z^2 + 2ie_y e_z\frac{k_y}{k}\right]J_x^2 + \left[-e_x^2\frac{k_x^2}{k^2} + e_y^2\frac{k_y^2}{k^2} + e_z^2 + 2ie_x e_z\frac{k_x}{k}\right]J_y^2\right)\ . \tag{S24}$$

To recover the current densities J_x and J_y, Eq. (S22) or Eq. (S24) must be inverted. Since J_x and J_y are connected via the continuity equation,

$$k_x J_x + k_y J_y = 0 \tag{S25}$$

knowledge of either $B_{||}$ or $B_\perp$ is sufficient to reconstruct the complete two-dimensional current density $\mathbf{J}$ (for $B_\perp$, only the absolute value can be reconstructed). The reconstructed current density from $B_{||}$ using Eqs. (S22) and (S25) is

$$J_x = \frac{w}{g\left[e_y - e_x\frac{k_x}{k_y} + ie_z\frac{k}{k_y}\right]}B_{||}\ , \tag{S26}$$

$$J_y = \frac{w}{g\left[e_x - e_y\frac{k_y}{k_x} - ie_z\frac{k}{k_x}\right]}B_{||}\ , \tag{S27}$$

where w is a window function whose purpose it is to dampen out noise at high spatial frequencies where g is small. We have used the Hanning window

$$w = \begin{cases} \frac{1}{2}\left[1+\cos(\pi k/k_{\max})\right] & \text{if } |k| < 2\pi/\lambda \\ 0 & \text{otherwise} \end{cases}\ , \tag{S28}$$

where λ is the spatial filtering parameter (with units of m) and $k_{\max} = 2\pi/\lambda$ is the associated cut-off wave vector. Likewise, the current density reconstructed from $B_\perp$ using Eqs. (S24) and (S25) is

$$J_x = \frac{w}{g_x}B_\perp\ , \tag{S29}$$

$$J_y = \frac{w}{g_y}B_\perp\ , \tag{S30}$$

with the inverse transfer functions

$$g_x = \left(\frac{g^2}{k_y^2} \sum_{i,j=x,y,z} \kappa_i \kappa_j \right)^{1/2} , \tag{S31}$$

$$g_y = \left(\frac{g^2}{k_x^2} \sum_{i,j=x,y,z} \kappa_i \kappa_j \right)^{1/2} , \tag{S32}$$

where

$$\kappa_x = i e_x k_x \ , \tag{S33}$$

$$\kappa_y = i e_y k_y \ , \tag{S34}$$

$$\kappa_z = e_z k \ . \tag{S35}$$

B. Image processing

Several image processing steps were found to significantly improve the quality of the image reconstruction. Starting with a raw image of $\delta\omega$ (or Ω, ϵ), key processing steps included:

1. The raw data was corrected for positional drift that occurred in the beginning and over long measurement periods. For this purpose, the topographic image recorded simultaneously with the magnetic image was compared to a separate reference AFM image. Each line scan (x scan) was then separately x-shifted to match the reference AFM image. Drift in y direction was not corrected. Drift was typically less than 50 nm over an entire scan.

2. The raw $\delta\omega$ and (Ω, ϵ) data were converted to units of magnetic field, $B_{||}$ and $B_{\perp}$.

3. A 3×3 pixel median filter was applied to reject outliers, *i.e.*, image points where the Lorentzian fit had failed. This most often occurred in areas where the microwave power was low and the EPR spectrum was barely resolved. The median filter was implemented as follows: For each pixel, it was checked whether the pixel value was larger (or smaller) than the value of the 8 surrounding pixels. If yes, the pixel's value was replaced by the median of the 8 surrounding pixels. This median filter was typically iterated 2-3 times and found to efficiently reject outliers. Excessive median filtering results in poorer image resolution.

4. The image canvas was extended by extrapolating experimental points outward. Two extrapolation methods were used: (i) A periodic boundary condition where the dataset was

mirrored at the edges of the image. This resulted in a 3×3-fold enlarged canvas. (ii) The values at the edges were projected outward and optionally dampened towards zero using a $\cos^2$ function when going further away from the edge. Canvas enlargements between 3×3 and 27×27 were used.

5. The image was deconvolved into a current density image.

6. The canvas of the current density image was cropped to its original size.

7. The current density image was interpolated by $1 - 16\times$ to a higher pixel resolution.

C. Spatial resolution

We defined the spatial resolution by the rise of the signal across a step edge. The distance over which the signal rises from 15% to 85% between its minimum and maximum values corresponds to about 2σ of the Gaussian convoluted with the step edge. The 2σ distance also coincides with the $\lambda/4$ distance of the cut-off wavelength. Hence, the quarter-cutoff-wavelength $\lambda/4$ has a special meaning, as it represents an absolute lower limit to the spatial resolution. Because the Hamming window suppresses high-frequency components already before reaching the cutoff wavelength, the spatial resolution observed in experiments is typically by a factor of two larger, of order $\lambda/2$.

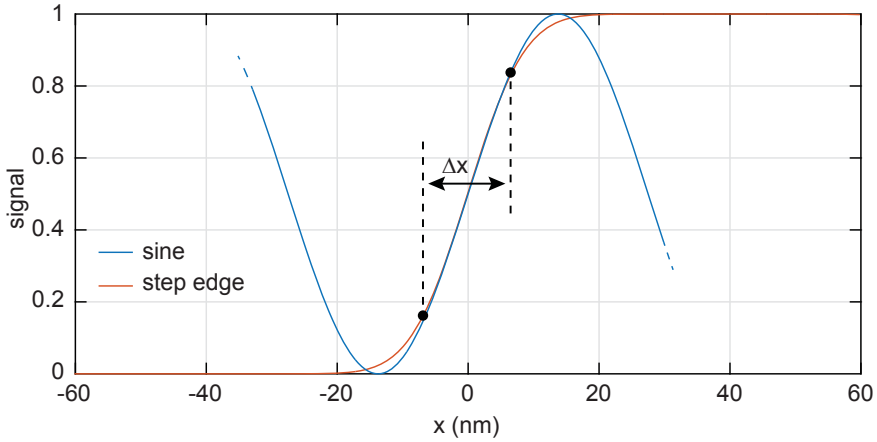

FIG. S3. Relation between wavelength parameter λ and spatial resolution. Red curve represents a step edge convolved with a Gaussian with $\sigma = \lambda/8 = 6.875\,\text{nm}$. Blue curve shows a spatial oscillation with wavelength $\lambda = 55\,\text{nm}$. The distance Δx over which the signal rises from 15% to 85% is approximately $\Delta x = 2\sigma = \lambda/4 = 13.5\,\text{nm}$.

D. Current density uncertainty

The noise in a reconstructed image was analyzed by inspecting an area of the image where no current density was expected. As the current density uncertainty we defined the standard deviation of $|J(x,y)|$,

$$\sigma_{|J|} = \frac{1}{A}\left[\int_{x,y} dxdy\,(|J(x,y)| - |\bar{J}|)^2\right]^{1/2} , \tag{S36}$$

where $|\bar{J}|$ is the mean value of $|J(x,y)|$ and A is the integrated area. If the noise in the area A is dominated by measurement noise (and not by artifacts caused by an improper reconstruction) then $\sigma_{|J|} \approx |\bar{J}|$. The reported current uncertainty corresponds to the current density uncertainty multiplied by the conductor cross-section,

$$\sigma_I = wh\,\sigma_{|J|} , \tag{S37}$$

where h is the conductor height and w is the lateral width of the integration. For the analysis in Fig. 4, $h = 100\,\mathrm{nm}$ and $w = 52\,\mathrm{nm}$.

IV. MICROWAVE SENSITIVITY DETERMINED VIA T_1 DECAY

We have used a T_1 experiment to determine the sensitivity to microwave currents [S8]. For this purpose, the magnetometer was operated in a time-resolved mode. A first ~ 3 μs laser pulse was used to pump the NV center into the $m_S = 0$ state and a second ~ 3 μs laser pulse was used to read out the final state after a variable waiting time t_1. During the entire measurement, a weak microwave current of ~ 50 μA was applied to the nanowire. We then performed a one-dimensional line scan across the nanowire as with Fig. 2 in the main manuscript.

Fig. S4 shows the optical contrast ϵ as a function of x position and waiting time t_1. By comparing the experimental data to a numerical simulation, we found a maximum Rabi frequency of 2.2 MHz, a detuning of the EPR resonance of $\Delta = 0.8$ MHz and the relaxation times $T_{2\rho} = 1$ μs and $T_1 = 35$ μs. The minimum detectable microwave field limited by T_1 would hence be $\sim 1\,\mathrm{nT}/\sqrt{\mathrm{Hz}}$ [S9]. In our experiment, however, the minimum detectable microwave field was limited by the detuning Δ, because the sensor's EPR frequency needs to be matched to the microwave frequency. The detuning of $\Delta = 0.8$ MHz converts to a magnetic field of $\Delta/\gamma \sim 30$ μT. Although smaller detunings can in principle be reached, this is hampered by the hyperfine interactions to the intrinsic nitrogen nucleus and nuclear ^{13}C spins, as well as temperature drifts.

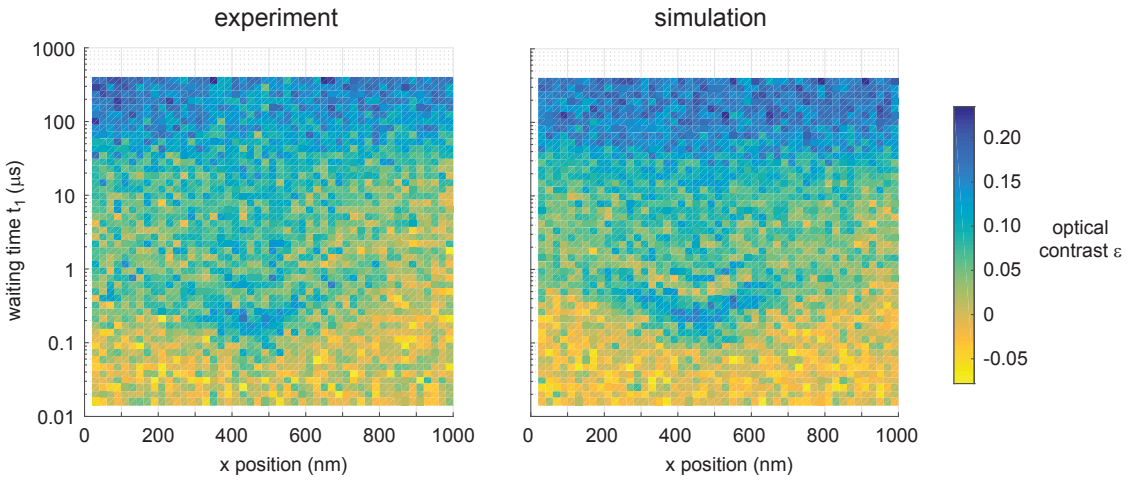

FIG. S4. Rabi measurement as a function of x position and waiting time t_1 while the NV center was scanned across a Pt nanowire located at $x = 450$ nm and $z = 85$ nm. Left plot shows the data and right plot shows a numerical simulation. Noise was added to the simulation to make it better resemble the experiment.

V. ADDITIONAL IMAGES

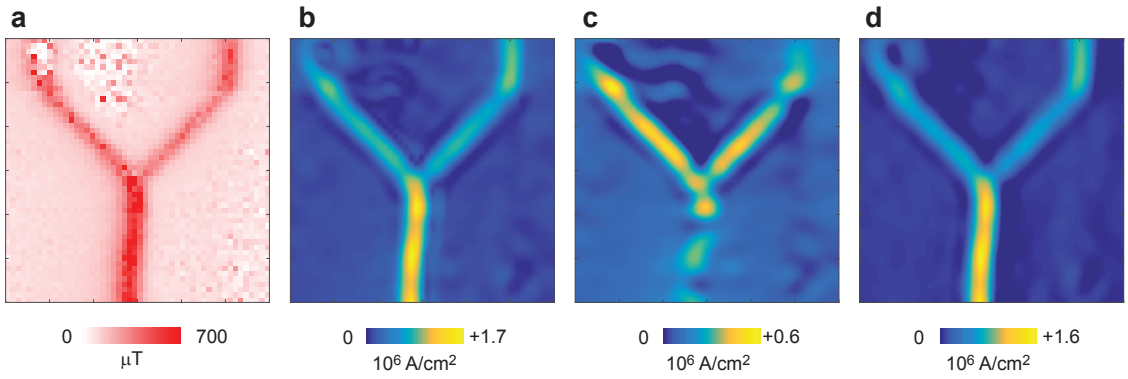

FIG. S5. **Current density reconstruction for the line width data from Fig. 3. a**, Line width Ω (same as Fig. 3c). **b**, Reconstructed current density $|\mathbf{J}(x, y)|$, using the same parameters as in Fig. 3. **c,d**, $|J_x|$ and $|J_y|$ components of current density. Image size is 3×3 μm^2.

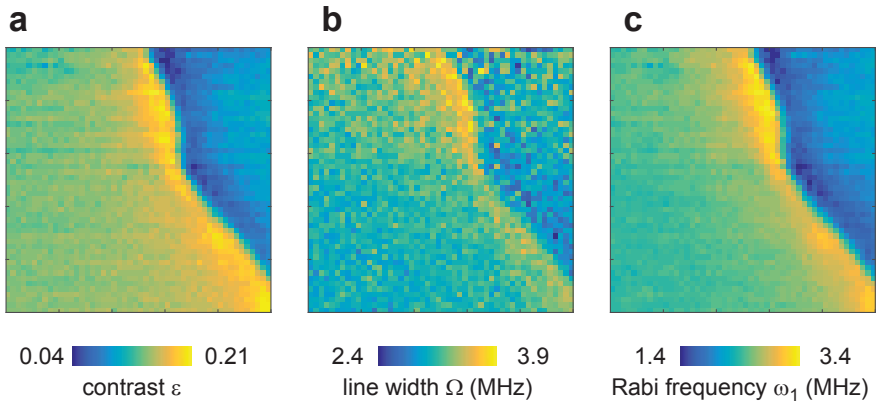

FIG. S6. **Supporting data for Fig. 5. a**, Optical contrast ϵ (same as Fig. 5c). **b**, Line width Ω. **c**, Rabi frequency ω_1 calculated according to Eq. (2) in the main manuscript using $\epsilon_{\max} = 0.23$. The line width data was low-pass filter prior to calculating ω_1. The transverse field is $B_\perp = \sqrt{2}\omega_1/\gamma$. Image size is 1×1 μm^2.

[S1] T. Rosskopf, J. Zopes, J. M. Boss, and C. L. Degen, arXiv:1610.03253 (2016).

[S2] S. K. Youn, N. Yazdani, J. Patscheider, and H. G. Park, RSC Advances **3**, 1434 (2013).

[S3] V. M. Acosta, E. Bauch, M. P. Ledbetter, A. Waxman, L. S. Bouchard, and D. Budker, Phys. Rev. Lett. **104**, 070801 (2010).

[S4] P. Wang, Z. Yuan, P. Huang, X. Rong, M. Wang, X. Xu, C. Duan, C. Ju, F. Shi, and J. Du, Nat. Commun. **6**, 6631 (2015).

[S5] A. Dreau, M. Lesik, L. Rondin, P. Spinicelli, O. Arcizet, J. F. Roch, and V. Jacques, Phys. Rev. B **84**, 195204 (2011).

[S6] K. Jensen, V. M. Acosta, A. Jarmola, and D. Budker, Physical Review B **87**, 014115 (2013).

[S7] B. J. Roth, N. G. Sepulveda, and J. P. Wikswo, J. Appl. Phys. **65**, 361 (1989).

[S8] P. Appel, E. Neu, M. Ganzhorn, A. Barfuss, M. Batzer, M. Gratz, A. Tschope, and P. Maletinsky, Rev. Sci. Instrum. **87**, 063703 (2016).

[S9] T. Rosskopf, A. Dussaux, K. Ohashi, M. Loretz, R. Schirhagl, H. Watanabe, S. Shikata, K. M. Itoh, and C. L. Degen, Phys. Rev. Lett. **112**, 147602 (2014).